The 2020 M$_w$ 6.5 Monte Cristo Range, Nevada earthquake: relocated seismicity shows rupture of a complete shear-crack system

Anthony Lomax[1]

[1]ALomax Scientific, Mouans-Sartoux, France. anthony@alomax.net Twitter: @alomaxnet

This is a preprint submitted to EarthArXiv. This manuscript was submitted 16-Oct-2020 for publication in a prominent scientific journal, where the manuscript was peer reviewed and rejected. If accepted by another journal, the published version will be linked to this EarthArXiv submission. Please feel free to contact the author with questions or comments.

Anthony Lomax

anthony@alomax.net

The 2020 M$_w$ 6.5 Monte Cristo Range, Nevada earthquake: relocated seismicity shows rupture of a complete shear-crack system

Anthony Lomax[1]

[1]ALomax Scientific, Mouans-Sartoux, France.

Corresponding author: Anthony Lomax (anthony@alomax.net)

ABSTRACT

The predominant model for earthquake faulting is a shear crack, including surrounding damage zones. Observation of this complete shear crack system at seismogenic depth, however, has been elusive. Shear cracks with damage zones are related to fault formation and growth, and earthquake rupture physics and size, but observational and analytical limitations impede use of the shear crack paradigm in quantitative, monitoring and hazard seismology. Here we obtain high-precision earthquake relocations for the 2020 M6.5 Monte Cristo Range, Nevada earthquake sequence. The seismicity illuminates two, en-echelon primary faulting surfaces and surrounding, characteristic shear-crack features such as edge, wall, tip, and linking damage zones, showing that this sequence ruptured a complete shear crack system. Shallow damage zones align with areas of dense surface fracturing, subsidence and after-slip, showing the importance of damage zones for shaking intensity and earthquake hazard. These results emphasize the importance of using the complete shear crack model in earthquake seismology.

INTRODUCTION

Earthquakes result from the release of elastic strain energy though slip across faults deep in the Earth. Fault segments can be idealized as shear cracks, with geometrical and energy constraints during slip and fault growth producing complex damage zones surrounding the crack. Geometrical and physical properties of the complete shear crack and damage zone system are directly related to fault formation and growth, and earthquake size and rupture propagation (*1–6*).

Shear cracks and faults are studied though theory, numerically, in the laboratory, at the surface through field investigation or remote sensing, and at depth through geophysical measures (*1, 3, 5, 7–20*). These studies characterize a complete system of shear-crack faulting (Fig. 1) as a high-strain core with a fracture damage zone halo and a broader, surrounding damage zone comprising edge, wall, tip, and linking faults and fractures (*2, 21–23*). Damage around fault edge tips, parallel to the main slip direction, includes en-echelon Riedel shears and complex palm or flower structures at shallow depth. Lateral tips, normal to the main slip direction, show damage primarily on the dilatational side of the fault, dominated by wing cracks and horsetail fractures with extensional slip, and synthetic branch faults or splay faults with slip similar to the main slip. Linking damage zones included extensional and contractional steps, show high complexity and often form through the fusion of lateral tip damage zones of adjacent shear cracks. Wall damage may include any of these features as abandoned relics of previous fault tip propagation. The high-strain core forms the principal slip surface in large earthquakes and typically hosts few

aftershocks, while the damage zones host a majority of aftershocks due to stress concentration and fault growth after main rupture (*19, 24–28*).
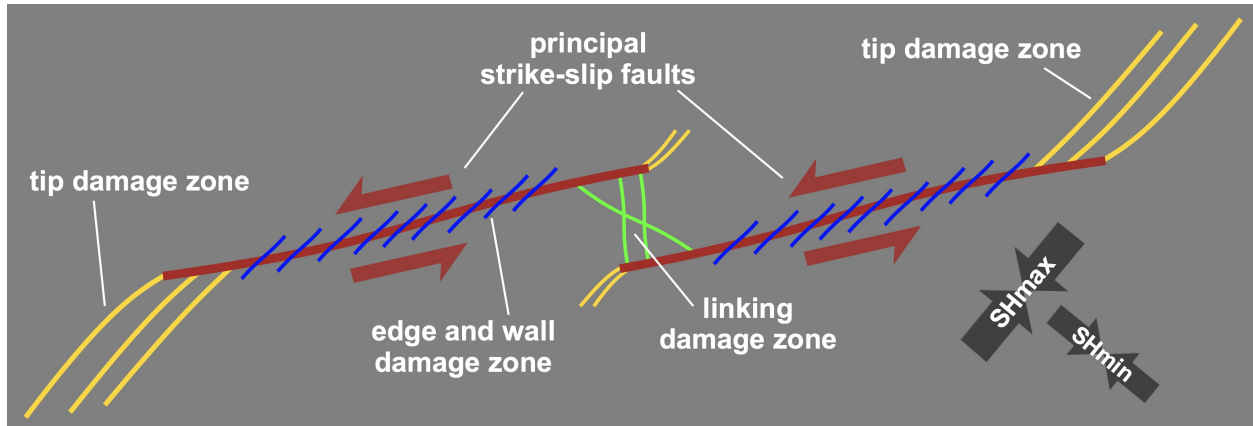

Fig. 1. A complete shear crack system. Schematic map view of shear-crack damage zones around left-lateral, strike-slip faulting cores separated by a contractional, linking stepover. SHmin and SHmax show directions of minimum and maximum compressive stress, respectively.

Though many large, hazardous faults are considered "mature", with cumulative slip of 10-100's of km and composed of few segments relative to their length (*6, 29*), seismicity on these faults usually does not clearly exhibit features of shear cracks other than a high-strain core. High-accuracy and high-precision earthquake relocations allow inference of three-dimensional faults geometry at seismogenic depths and sometimes resolve apparent shear-crack features, such as tip, linking or wall damage zones, step-overs, and orthogonal antithetic faulting, as components of overall faulting patterns in complex or diffuse seismicity (*30–38*). Identification of a majority of the primary slip surfaces and aftershock seismicity for a large-earthquake at seismogenic depth with the expected geometry and features of a complete shear-crack system would clearly emphasize how earthquakes are rupture of shear cracks, and should be modeled as such to advance quantitative, monitoring and hazard seismology.

The 2020-05-15, M_w 6.5 Monte Cristo Range, Nevada earthquake occurred in western Nevada in the Mina deflection, a major structural right-step with block rotation and east-northeast trending sinistral faulting within the northwest trending, dextral, eastern California shear zone to Walker Lane belt system (*39, 40*). Left-lateral, strike-slip faulting on a steep, N73ºE striking plane for the M_w 6.5 mainshock is indicated by the distribution of aftershocks and by the USGS, W-phase centroid moment tensor (USGS-CMT; Hayes et al., 2009; Benz, 2017), the Nevada Seismological Laboratory (NSL) regional moment tensor (NSL-RMT; *41*), and other mechanism solutions. The Monte Cristo event has a productive aftershock sequence (over 12,000 events detected up to 2020-07-31), while numerous nearby stations, a low-noise monitoring environment, and high-quality event detection, processing and data archiving at the NSL, USGS and IRIS Data Management Center (IRIS-DMC) make this sequence an excellent opportunity for high-precision aftershock relocation to resolve detailed, 3D features of seismicity for a large earthquake.

Here we obtain high-precision, absolute earthquake relocations for Monte Cristo seismicity from 2020-01-01 to 2020-07-31 using a robust, probabilistic location method (*42*, *43*), source-specific, station travel-time corrections, and a new, multi-event, absolute relocation procedure based on waveform coherency between events. These procedures produce a detailed, 3D map of the Monte Cristo seismicity and associated focal mechanisms which we interpret as numerous shear-crack features, including edge and lateral tip damage zones, and a contractional stepover. This seismicity delimits two principal slip surfaces for mainshock rupture, though few events locate on these surfaces, and a broad zone of shallower, secondary strike-slip and damage zone faulting to the west. This high-precision, 3D seismicity characterizes the M_w 6.5 Monte Cristo rupture as faulting on a complete but relatively simple set of shear-crack structures.

MATERIALS AND METHODS

Earthquake catalog

We obtain an earthquake catalog for the Monte Cristo area (latitude 37.76º to 38.59º, longitude -118.62º to -117.27º) from 2020-01-01 to 2020-07-31 through earthquake.usgs.gov (*44*) including corresponding NSL and USGS P and S arrival times, time uncertainties and first-motions. This USGS-NSL catalog (Fig. S2) contains about 12,000 events down to M-0.2 and is complete down to about M1.5. We obtain from IRIS-DMC metadata for permanent and temporary stations used for relocation (within 1º of latitude 38.16º, longitude -117.88º; near the M_w 6.5 epicenter) and waveforms for coherence analysis.

High-precision, absolute relocation

Accurate and precise absolute location of earthquake hypocenters requires stations close to and above the source zone with high-quality, consistent arrival-time picking (*45–48*), using 3D and geology-based, seismic velocity models (*49–52*), calibrating arrival-time corrections with ground-truth sources (*53*, *54*), application of station travel-time corrections (*55–59*), and use of location algorithms robust to error in the velocity models or earthquake arrival-time data (*43*, *57*, *60*). High-precision, multi-event, relative location (*60–65*) requires and builds upon accurate, precise absolute location by using waveform similarity and cross-correlation timing to gain information on fine-scale, inter-event spatial relations.

We obtain absolute earthquake relocations for the Monte Cristo area using source-specific, station travel-time corrections (SSST; *56*) and high-precision relocation based on waveform coherency between events. These procedures produce enhanced relative location and clustering of events, and allow analysis of model- and data-dependent error in the hypocenters.

We perform these relocations with the NonLinLoc (NLL) algorithm (*42*, *43*), which uses efficient global sampling algorithms to obtain an estimate of the posterior probability density function (PDF) in 3D space for absolute hypocenter location. The location PDF provides a complete description of likely hypocentral locations, includes comprehensive uncertainty information, and allows robust application of waveform coherency relocation. Within NLL, we use the equal differential-time (EDT) likelihood function (*43*, *57*, *66–68*), which is very robust in the presence of outlier data caused by large error in the arrival-times or predicted travel-times.

For initial NLL relocations we calculate travel-times in a smoothed version (KS-smooth; Fig. S1) of the KS seismic P-wave velocity model used for 2008 Mogul, northwest Nevada sequence relocations (*69*); a smooth model avoids location artifacts at layer interfaces. We use a finite-differences, eikonal-equation algorithm (*70*) to calculate P travel-times for each station and use a constant Vp/Vs=1.73 to obtain S travel-times.

We relocate events in two stages using NLL. For the first stage, starting with the initial NLL relocations (Fig. S2), we iteratively generate SSST corrections which vary smoothly within a 3D volume to provide a source-position dependent correction for each station and phase type. We use smoothing distances of 32, 16, 8 and 4km and only events in the USGS-NLL catalog which have arrival data at one of the nearby temporary stations, installed from 2020-05-16. Only P and S arrivals with residuals of ≤1.0 sec for relocated events meeting minimum quality criteria are used for update at each iteration. See supplementary material Methods S1 for more details. We relocate the full catalog using the final 4km smoothing-length, SSST corrections (Fig. S2). The median formal error (e.g. with velocity model fixed) for the NLL-SSST relocations is 1.5 km in epicenter and 1.7 km in depth.

In the second relocation stage we greatly reduce absolute location, aleatoric error by combining location information across events based on waveform coherency between the events. This absolute coherency relocation is based on the concept that if the waveforms at a station for two or more events are very similar (have high coherency) up to a given frequency, then the distance separating these "multiplet" events is small relative to the seismic wavelength at that frequency and the events represent stress release on the same, small fault patch (*71–73*). The NLL coherency relocation for a target event is a stack over 3D space of the event's SSST location PDF and the SSST PDF's for other events, each weighted by the waveform coherency between the target event and the other event. The same weighting is used to combine first-motion readings between multiplet events, producing an increased number of more robust, though locally correlated, focal-mechanisms. Unlike differential-time based relative location, absolute coherency relocation requires waveforms from only a single stations, allowing precise relocation for sparse networks, and for foreshocks and early aftershocks of a mainshock sequence or swarm before temporary stations are installed. See the supplementary material Methods S2 for more details. The median formal error for the final NLL-SSST-coherence relocations is 0.33 km in epicenter and 0.35 km in depth. A comparison with relocations using the smooth KS model modified with lower and higher velocities gives an estimate of epistemic absolute error of about 1 km in epicenter and 1.5 km in depth, with events shifted shallower and to the south in the faster model.

We relocated the M_w 6.5 mainshock hypocenter using the final SSST corrections and arrivals picked arrivals on waveforms obtained from IRIS-DMC to augment the USGS and NSL arrival data. Since nearby temporary stations are not available and waveforms for the large mainshock do not correlate with any later events, the mainshock hypocenter is poorly constrained in depth at 12±8km, while the epicenter is moderately well constrained within ±2 km. Mainshock relocation with and without S arrival readings give similar epicenters but no depth constraint (Table 1; all depths in this study are below sea level).

Table 1. M_w 6.5 Monte Cristo foreshock and mainshock relocations

Origin time (UTC)	Event	Mag	Lat	Long	errH	Depth
2020-01-26 02:25:52.3	Foreshock (well constrained)	1.8	38.156°	-117.894°	±0.4km	8.1±0.2km
2020-03-12 08:13:09.2	Foreshock (well constrained)	2.2	38.156°	-117.893°	±0.7km	8.1±0.2km
2020-03-12 08:21:22.3	Foreshock (well constrained)	1.1	38.156°	-117.883°	±0.7km	8.1±0.2km
2020-03-30 20:55:56.5	Foreshock	1.0	38.156°	-117.901°	±2.0km	5.4±7.2km
2020-03-31 05:43:20.9	Foreshock	1.1	38.148°	-117.872°	±2.2km	4.1±10.5km
2020-05-15 11:03:27.1	Mainshock P+S	6.5	38.162°	-117.890°	±1.7km	12.2±7.5km
2020-05-15 11:03:26.9	Mainshock P only	6.5	38.175°	-117.895°	±2.7km	1.8±6.0km
	Mainshock proxy	6.5	38.156°	-117.890°		8.1 km

RESULTS

Monte Cristo sequence seismicity and interpreted faulting structures

We examine the Monte Cristo sequence seismicity in detail using NLL-SSST-coherence absolute relocations of the 2020-01-01 to 2020-07-31 USGS-NSL catalog. Aftershock seismicity may outline principal rupture surfaces or define surrounding damage zone structures, or may be triggered or induced events on secondary structures at some distance from the principal rupture zones (*6, 26, 74, 75*). We attempt to distinguish and identify these cases here though analysis and classification of seismicity patterns and focal mechanisms.

Fig. 2 shows a map view of the relocated seismicity, with moment tensor mechanisms and surface observations relating to the Monte Cristo sequence and a large earthquake in 1932, and contextual geologic and geophysical information. Most Monte Cristo seismicity falls along an ~45 km long and ~5 km wide, ~N75°E trending, near-vertical zone, with the majority of events distributed from ~14 km east to ~20km west of the mainshock epicenter and within about 1-12 km depth. This main trend matches the strike of the near east-west fault plane of the USGS-CMT and the NSL-RMT moment tensors for the mainshock. Much of the seismicity forms sparse clusters of about 100 m extent or less, or forms narrow, elongated, tabular groupings up to about 500 m long. This sparseness and grouping shows the prevalence in this sequence of multiplet events for which coherence relocation finds nearly coincident hypocenters with an apparent inter-multiplet relative error of less than 100 m.
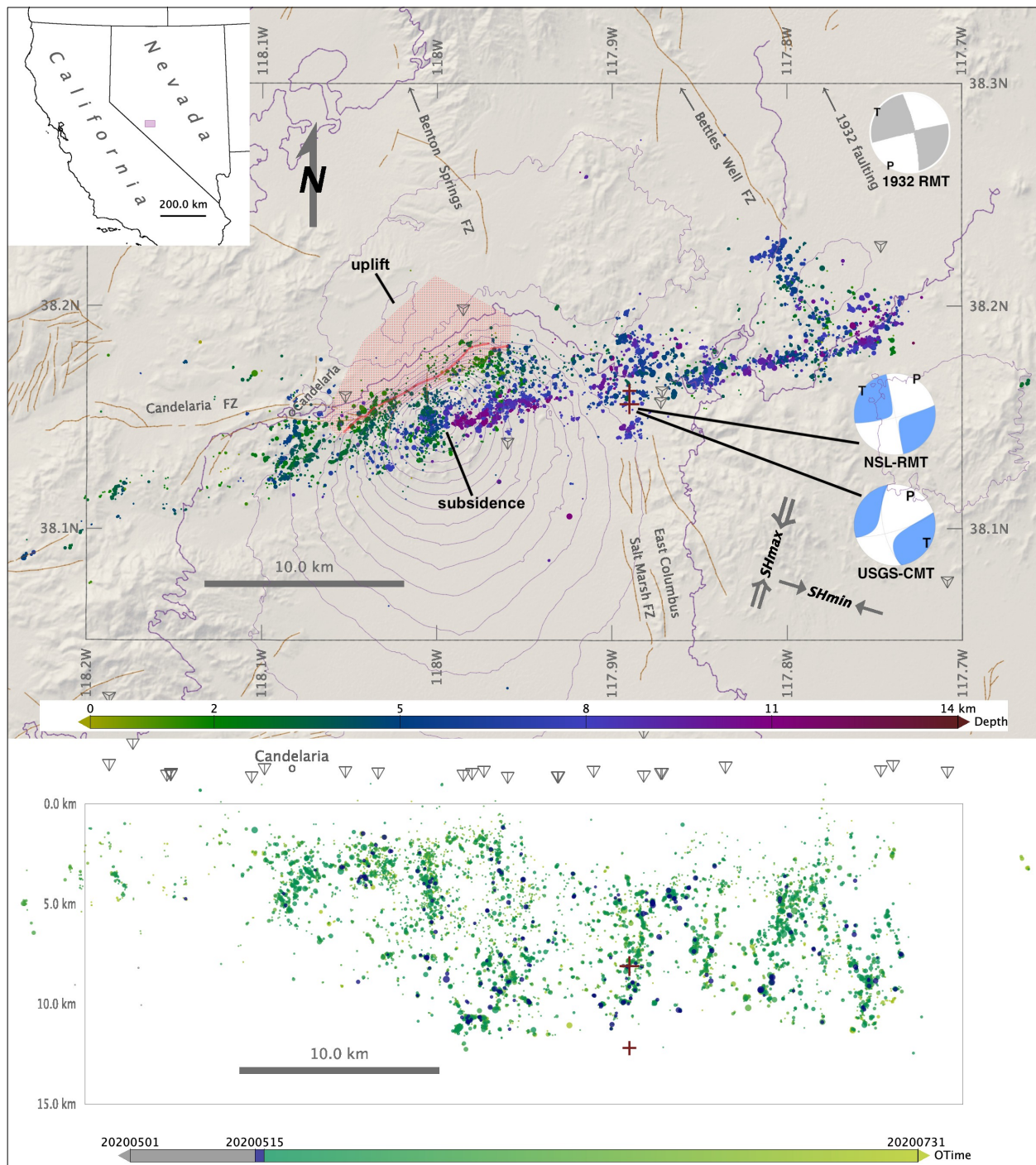
Fig. 2. Map view of Monte Cristo seismicity. NLL-SSST-coherence absolute relocations for ~11,000 events 2020-01-01 to 2020-07-31 with error-ellipsoid, semi-major axis ≤ 5 km. Map view with event color showing hypocenter depth and symbol size proportional to magnitude. Re-picked Mw6.5 hypocenter and its proxy (mean hypocenter of 3 well constrained foreshocks) indicated by small and large, dark red, cross symbols, respectively. Blue focal mechanisms show M_w 6.5 mainshock USGS-CMT W-phase and

NSL-RMT regional moment tensors, gray mechanism shows the RMT for the 1932 Mw 7.2 Cedar Mountain earthquake (*41*). Purple contours show Sentinel-1 vertical displacement (2 cm interval; heaviest contour indicates zero level; ~28 cm maximum subsidence; ~4 cm maximum uplift), thick, light red line shows interpreted NE-SW after-slip (May 17 – May 23) with 2-3 cm of LOS displacement (*76*). Red shade shows area of dense mapped surface ruptures and fractures (*77*). SHmin and SHmax show directions of regional minimum and maximum compressive stress, respectively (from 3 closest data in *81*); the intermediate principal stress axis is vertical. Seismic stations shown as dark gray tetrahedrons. Brown lines show faults from the Quaternary fault and fold database for the United States. Background topography image from OpenTopgraphy.org. Inset shows location of study area (blue rectangle) in the western United States. The lower panel shows a depth-distance view from south with event color showing origin time (dark blue shows events in first day after the mainshock) and symbol size proportional to magnitude. See also in the electronic supplement to this article Movie S1 (available here during review: http://alomax.free.fr/projects/MonteCristo_2020/MonteCristo2020_ALomax_NLL-SSST-coherence_movie.mp4).

In map view, two, distinct, linear, deeper zones of seismicity parallel to the main trend extend ~12km east and west from the epicentral area. Within about 3 km of the epicenter the seismicity suggests additional faulting structures north and south of the main trend. From about 5 to 18km west of the epicenter is a wide zone of shallow seismicity including southwest-northeast lineations, the westernmost of this seismicity under Candelaria and further to the west-southwest activates a day or more after the mainshock (Fig. 2). About 4 km west of the eastern end of the aftershock zone and perpendicular to the main trend is an ~5 km long zone of seismicity crossed at its northern end by an ~2 km, orthogonal trend of epicenters. At the eastern end of the aftershock zone is a complex zone of seismicity to the northeast of the main trend. We examine further this seismicity along with focal mechanisms with consideration of their 3D geometry to show numerous shear-crack phenomena and provides details of the principal, damage zones and shallower rupture during and after the mainshock.

Principal slip surfaces

In 3D, the two, deeper, linear zones of seismicity parallel to the main trend consist of small clusters and short lineations of events on and around two, narrow (< 0.5km), en-echelon, surfaces extending ~12 km east and ~10 km west from the mainshock epicenter and from about 4-12km depth (Figs. 2 and 3). The eastern zone forms a near-vertical plane while that to the west is near-vertical below about 7 km and widens around a steep, ~70º south-southeast dipping plane at shallower depths (Fig. 4), possibly extending up to about 2 km depth at its western end. We interpret these zones as two principal slip surfaces for mainshock rupture. The deepest seismicity along these two slip surfaces (Fig. 3c; >9km) forms two distinct lineations offset by a right step of about 1.5 km, implying a contractional stepover for left-lateral faulting on the two surfaces. The small clusters and short lineations around these zones suggest Riedel shears, which are expected along fault edge tips of a shear-crack (*19*), though the precision of the relocations is not high enough to confirm this interpretation.
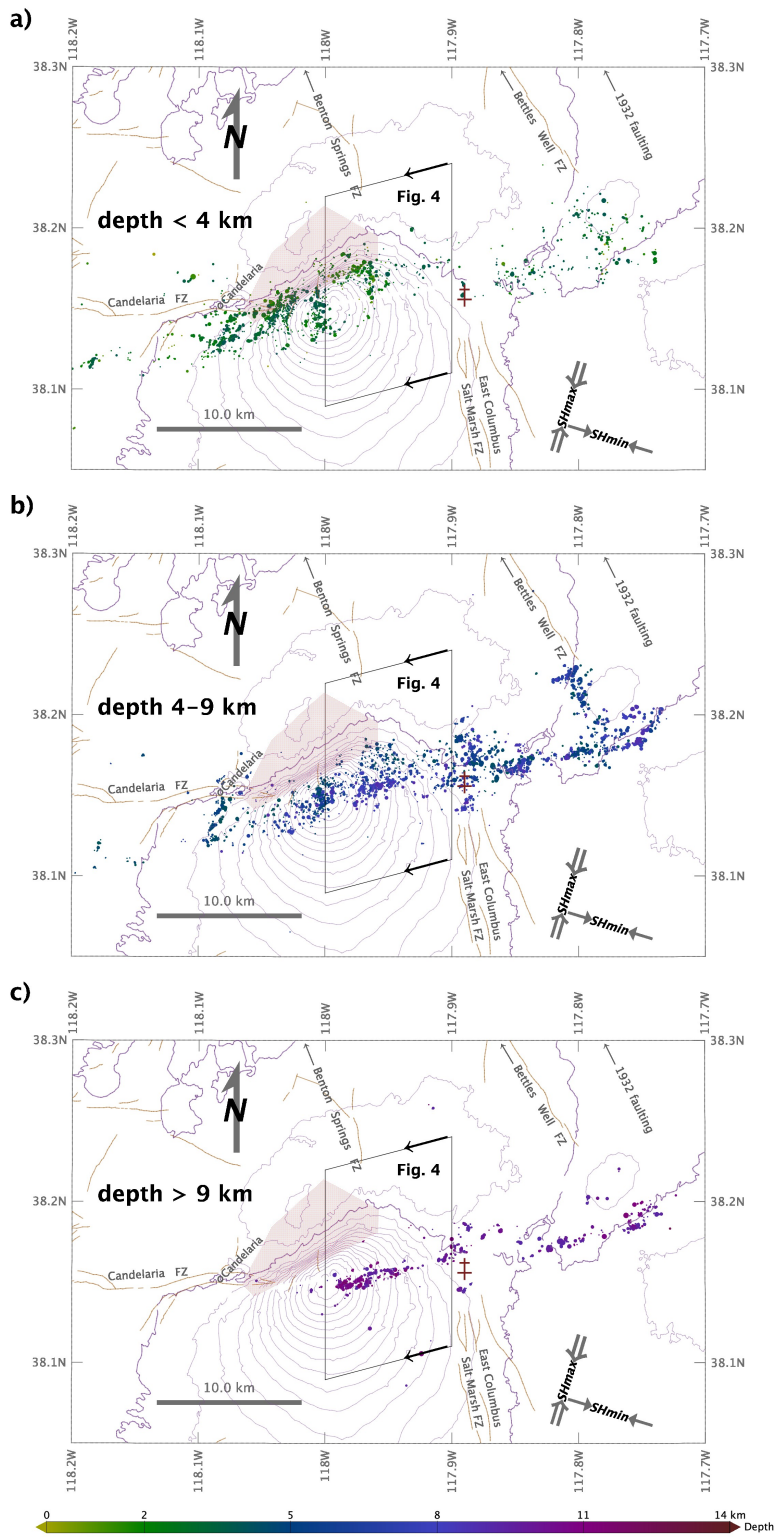
Fig. 3. Depth slices of Monte Cristo seismicity. NLL-SSST-coherence absolute relocations in depth ranges a) above 4 km, b) 4-9 km, c) below 9 km. Event filtering and map
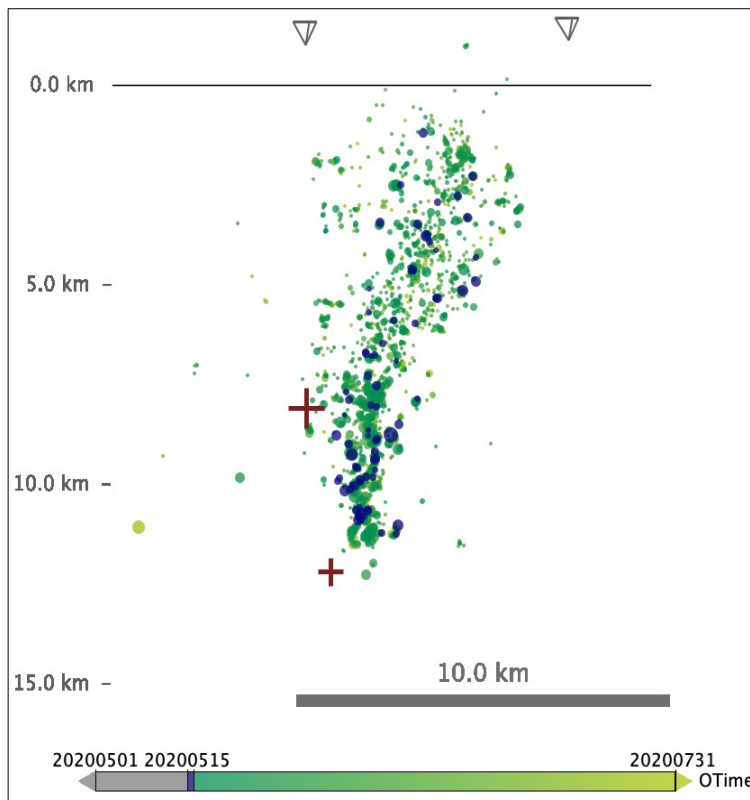
elements as in Fig. 2.

Fig. 4. Vertical section through western principal slip zone. Depth-distance view from N73ºE of NLL-SSST-coherence absolute relocations within the polygon shown in Fig. 3. Mw6.5 hypocenter and its proxy (dark red crosses) are projected from ~1 km east of section. Event filtering and map elements as in Fig. 2.

The eastern and western ends of each principal surface abut zones of seismicity to the northeast and southwest, respectively, of the trend of the surfaces, thus in the dilatational quadrant for sinistral faulting. (Fig. 5). Note that the western part of the western principal slip zone is dipping and offsets to the north at shallow depth, so the majority of shallow seismicity to the west (Fig. 3a; <4km) is in the dilatational quadrant of this slip surface. The zones of seismicity abutting the principal slip surfaces exhibit lineations striking about 40º counterclockwise to the strike of the principal slip surfaces and sub-parallel to the regional maximum compressive stress (Shmax). Events in these zones show normal-faulting mechanisms, indicating northwest-southeast extension, sub-parallel to the regional minimum compressive stress (SHmin), and strike-slip mechanisms with pressure and tension axes aligned with SHmax

and SHmin, respectively (Fig. 6). All of these characteristic are those expected for lateral tip damage structures (*2*, *78*).

Overall, the two principal slip surfaces and terminating damage structures bear a remarkable resemblance, on a large scale, to shear cracks with associated tip damage zones, with some additional complexity, particular at shallower depth for the western segment (Figs. 5 and 7).
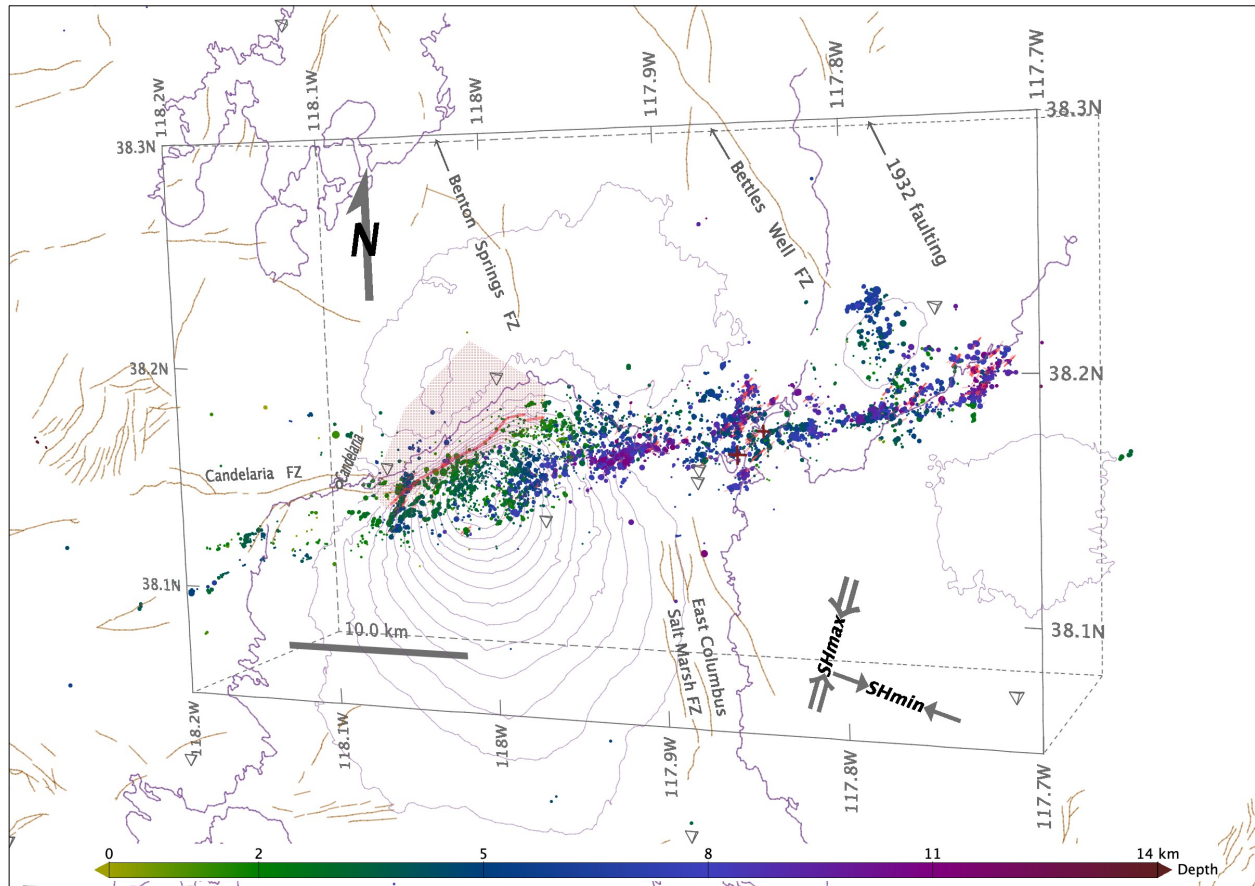

Fig. 5. Oblique view of Monte Cristo seismicity. NLL-SSST-coherence absolute relocations in perspective view downwards from east-northeast to align with main fault planes and fault tip damage structures. Red line segments show focal-mechanism nodal-axes for normal-faulting events; these axes fall approximately along the strike of the fault planes. Event filtering and map elements as in Fig. 2.
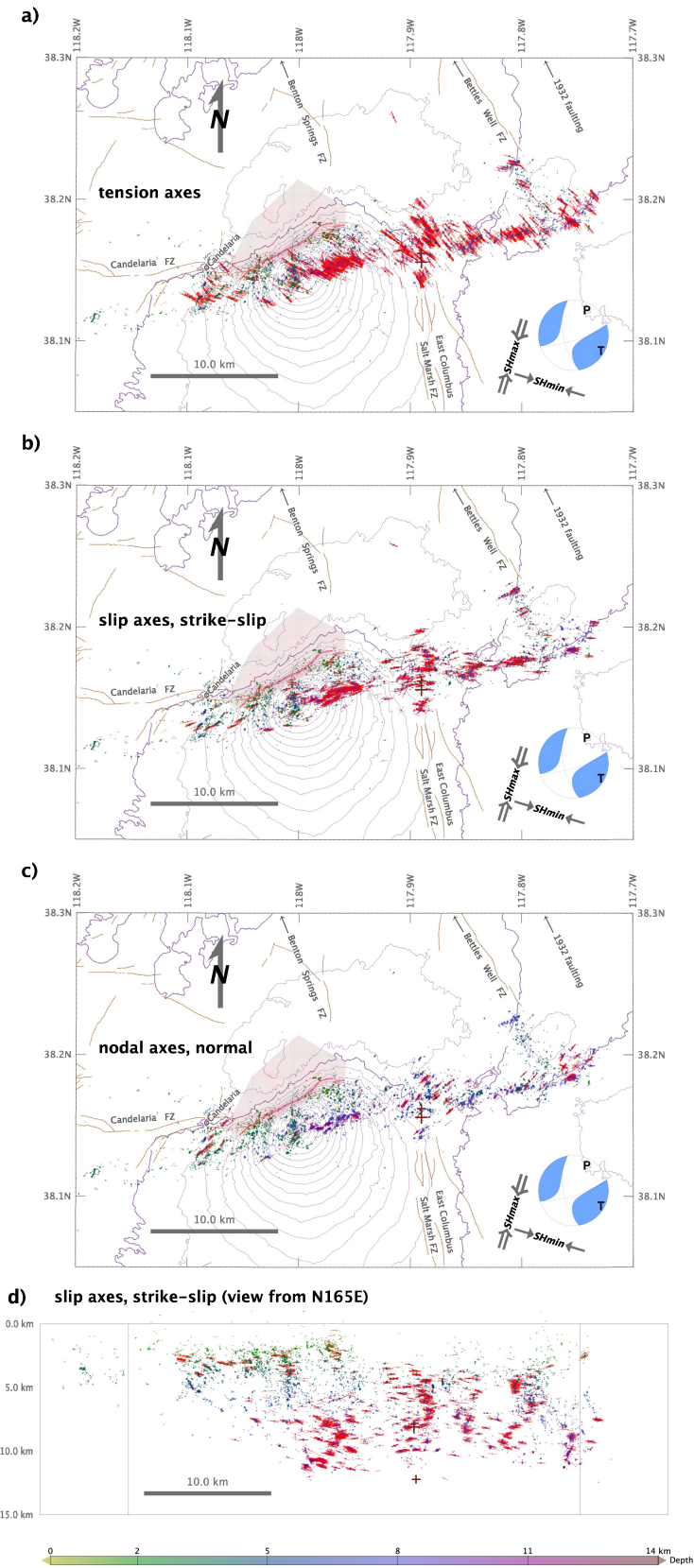
a) tension axes

b) slip axes, strike–slip

c) nodal axes, normal

d) slip axes, strike–slip (view from N165E)

Fig. 6. Tension axes and faulting orientations from Monte Cristo seismicity first-motion mechanisms. a) Focal mechanism tension axes for strike-slip and normal-faulting events. b) Focal mechanism slip axes closest to strike N73°E for strike-slip events; in map view these axes fall approximately along the strike of the faulting plane or of the auxiliary plane (i.e. the true fault-plane strike may be orthogonal to this axis). c) Focal mechanism nodal axes for normal-faulting events; these axes fall approximately along the strike of the faulting plane. d) Depth-distance view from N165°E (approximately perpendicular to main trend of seismicity) showing focal mechanism slip axes closest to strike N73°E for strike-slip events; in this view these axes fall approximately along the slip direction of the faulting plane or of the auxiliary plane (i.e. the true slip direction may be orthogonal to this axis). FMAMP focal mechanisms (supplementary material Methods S3) shown for events with ≥25 combined first-motion readings from multiplet events. Strike-slip events are defined as having nodal axis within 30° of vertical; normal-faulting events as having pressure axis within 30° of vertical and tension axis within 30° of horizontal; under similar criteria there are only around 10 thrust mechanisms (not shown or analyzed). NLL-SSST-coherence absolute relocations are shown with event color corresponding to hypocenter depth. Re-picked Mw6.5 hypocenter and its proxy (mean hypocenter of 3 well constrained foreshocks) indicated by small and large red cross symbol, respectively. Other map elements as in Fig. 2.

Mainshock hypocenter and rupture initiation

The mainshock hypocenter falls within the contractional stepover between the two principal slip surfaces (e.g. Fig. 3bc), but its large depth uncertainty precludes detailed association with faulting structures. There are, however, 5 likely foreshocks M 1.0-2.2 in the catalog within the Monte Cristo seismicity and near the mainshock epicenter (Table 1; Fig. S3). Three of these events are members of multiplets and have well constrained coherence locations, their hypocenters form a tight cluster within the contractional stepover at about 8km depth, above the mainshock hypocenter (Fig. 2). Since small foreshocks of large mainshocks in the eastern California shear zone and elsewhere are often nearly co-located with the mainshock hypocenter (*58, 79, 80*), we take the mean hypocenter of the 3 well constrained foreshocks as a well constrained proxy for the mainshock hypocenter (Table 1).

This proxy mainshock hypocenter is located near the western end of the eastern principal slip surface and in a tabular, north-south oriented zone of seismicity below about 4 km depth Figs. 2 and 3). This north-south zone links the ends of the two principal slip surfaces across the contractional stepover (Figs. 5 and 6). The focal mechanisms in this tabular zone are mainly strike-slip (Fig. 6) with either near east-west fault planes, giving left-lateral, synthetic faulting, or near north-south fault planes, giving right-lateral, antithetic faulting and perhaps counter-clockwise block rotation within the stepover. Around the north and south limits of this zone are clusters of events with mechanisms indicated northwest-southeast extensional faulting (northeast-southwest nodal axes in Figs. 4 and 5c; northwest-southeast tensional axes in Fig. 5a), this seismicity could define tip damage for the stepover faulting and the principal slip surfaces.

The proxy mainshock hypocenter allows that the mainshock initiated either as left-lateral rupture on the western end of the eastern principal slip surface, or right-lateral rupture on the north-south linking zone. It is also possible that the hypocenter corresponds to an immediate

foreshock on one of these structures that incited nearby rupture on the other structure or on the western principal slip surface.
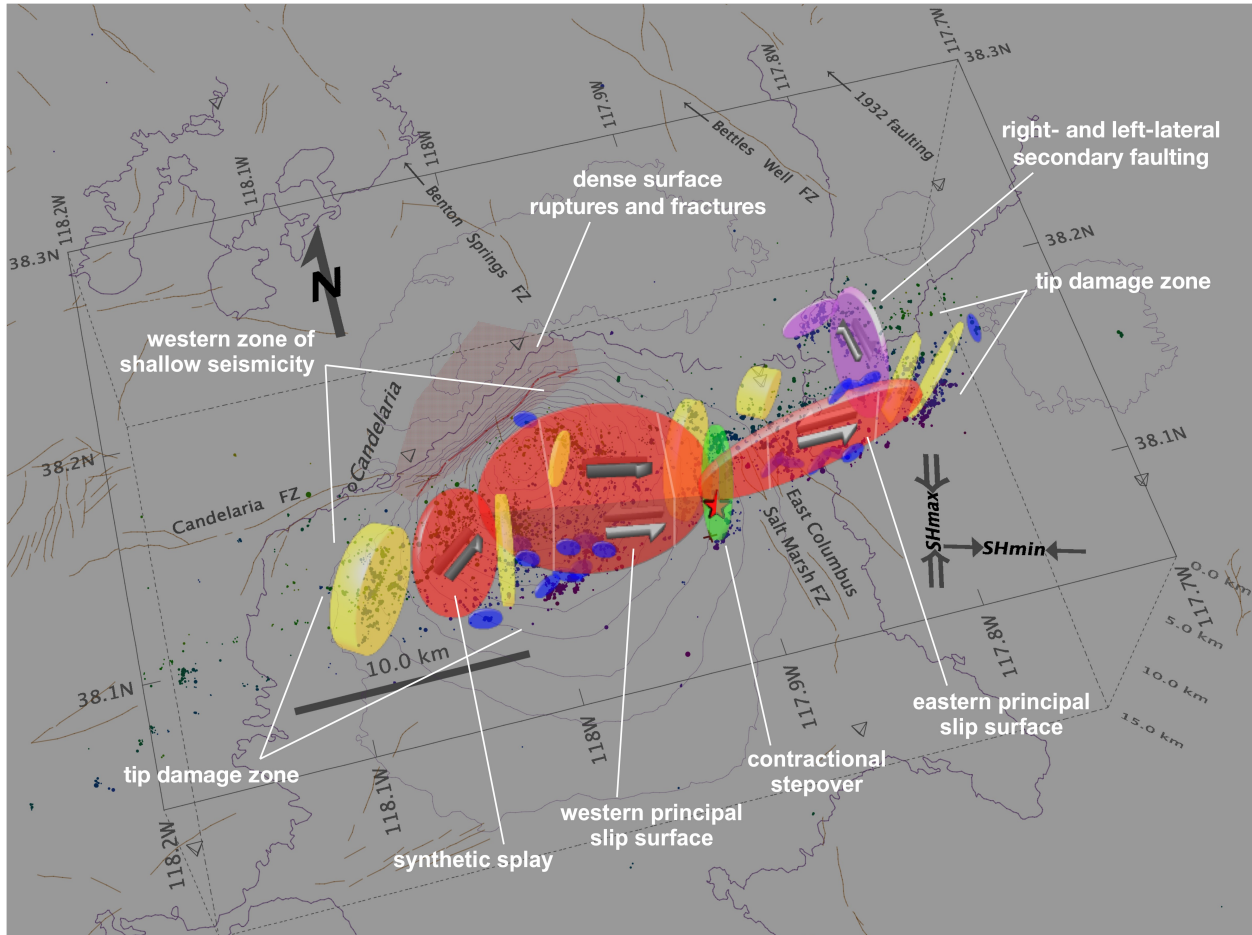

Fig. 7. Schematic interpretation of Monte Cristo seismicity. Perspective view downwards from the south-southwest showing NLL-SSST-coherence absolute relocations and simplified interpretations of primary fault planes, main fault damage zones and surface fracturing. Red star shows the proxy, mainshock hypocenter (Table 1). Orange shapes show the two, principal, left-lateral slip surfaces and the western, shallow, synthetic splay; green shape shows faulting across the contractional stepover; yellow shapes show selected tip damage zones consisting of mainly right-lateral, synthetic branch faults and extensional, horsetail splays; blue shapes show a sample of, mainly strike-slip, tip, upper and lower edge and wall damage zones including possible Riedel shears; purple shapes show likely triggered, right-and left-lateral secondary faulting. Event filtering and other map elements as in Fig. 2.

Orthogonal faulting to the east

Near the eastern end of the aftershock zone and perpendicular to the main trend is an ~5 km long linear trend of seismicity which aligns with unnamed faults further to the northeast

along the Pilot Mountains and the Bettles Well fault zone (Fig. 2). This perpendicular trend is terminated to the north by an ~2 km long, orthogonal lineation of events which activates 1 week after the mainshock with an M_w 5.1 event at 2020-05-22 00:22; the strike of this lineation matches closely the strike for left-lateral faulting in the M_w 5.1 USGS-CMT. Events in both of these trends have strike-slip focal mechanisms which, if the faulting planes follow the strike of the lineations, show right-lateral faulting for the longer trend and left-lateral faulting for the shorter trend (Fig. 6).

Shallow seismicity to the west

From about 5 to 18km west of the mainshock epicenter is an ~5km wide zone of shallow seismicity between ~1-7km depth (Figs. 3 and 4). The position and extent of of this seismicity, excepting the westernmost ~3 km which mainly occurred more than 2 days after the mainshock, corresponds to the main subsidence lobe and NE-SW trend of after-slip identified in the vertical Sentinel-1 InSAR LOS displacement, and to the upward tilted, dilatational quadrant of the USGS-CMT (Figs. 2 and 5).

This shallow seismicity includes the shallower, south-dipping part of the western principal slip surface (Fig. 4), which explains the asymmetry in vertical displacement lobes as the dipping fault plane is near the Earth's surface under the southern lobe and much farther from the surface position of the northern lobe. The shallow part of the western principal slip surface is joined to the west by a more counter-clockwise, southwest-northeast oriented, near-vertical, tabular zone of seismicity with almost exclusively strike-slip, aftershock focal mechanisms (Fig. 6b and 7), interpreted here as a major synthetic splay. East and west of this splay, shallow, southwest-northeast oriented seismicity with strike-slip and extensional faulting on apparent horsetail splays with strike ~30º counterclockwise to the main trend defines apparent lateral-tip damage structures. The apparent strike and dip of this inferred, shallow faulting agrees with the orientation of mapped normal and strike-slip faults in the Candelaria Mining District (*81*).

DISCUSSION

We have determined and analyzed high-precision, absolute earthquake relocations and focal mechanisms for the 2020 Monte Cristo earthquake sequence. The seismicity and focal mechanisms show mainshock rupture and aftershocks on two, principal, en-echelon slip surfaces, on major synthetic and antithetic faults, on splays, and in surrounding damage zones (Figs. 5 and 7), all of which characterizes a complete shear-crack system.

Our results suggests a rupture scenario with foreshock and mainshock hypocenters at about 8 km depth within the contractional stepover between the two principal, left-lateral slip surfaces, on synthetic or antithetic faulting within the stepover or on the eastern principal slip surface (Fig. 7). Rupture near the hypocenter transferred to or incited (*58*) rupture on the near vertical, deeper part of the western and eastern principal slip surfaces. Westward rupture propagated upwards onto the shallow, south-dipping segment of the western slip surface, and then onto the shallow, southwest-northeast striking, major synthetic splay.

Further Monte Cristo rupture, along with aftershocks and possible after-slip, occur on the edge, wall, tip, and linking damage zones of the principal slip surfaces, and on secondary structures, including the orthogonal, ~5 km long linear trend of seismicity near the eastern end of

the aftershock zone (Fig. 6). Orthogonal to this trend, an ~2km long streak of seismicity activates days after the mainshock, as does the westernmost ~3 km of the western zone of shallow seismicity and shallow seismicity further to the west-southwest. The seismicity does not reflect several, north-south oriented, surface mapped fractures with <10 cm of right-lateral offset above the principal slip surfaces (*77*). These fractures may be antithetic faults, expected above the top edge of deeper, strike-slip shear-cracks (*18*), and are probably not associated with seismicity since too shallow to host brittle faulting.

The 2020 Monte Cristo sequence occurred on previously unidentified and mostly buried or blind faults. However, the two, ~10-12 km long, principal slip surfaces separated by a compression right-step for Monte Cristo faulting resembles segment lengths and sense of offset observed at the surface for the Candelaria fault system (*82*), directly to west of and along the same trend as the Monte Cristo seismicity. The eastern limit of the Monte Cristo seismicity is about 15 km south-southeast of and aligns with the southernmost surface ruptures of 1932, Mw 7.2 Cedar Mountain earthquake (Fig. 2) (*83*).

Major strike-slip faults such as the San Andreas or North Anatolian have large geologic offset but few steps and other damage zone features per unit length, these are termed "mature" faults and likely represent the coalescence of earlier, short fault segments (*29*, *84*). The Monte Cristo seismicity shows that 2020 rupture involved two primary shear-crack fault segments with numerous and extensive damage features. These segments are unlikely to be mature, since the Mina deflection tectonic context limits maximum fault length and possibly maximum offset and age. However, irregular rupture and rupture termination in damage zones is likely responsible for large ground shaking, since fault tips, edges, bends, step-overs and associated damage zones radiate the strongest and highest frequency seismic waves (*85–88*) and host most aftershocks (*13*, *89*).

The position and depth of the mainshock proxy hypocenter, the slip rake from the USGS-CMT and other teleseismic CMT faulting mechanisms, the dip of aftershock slip axes and the shallow seismicity to the west (Figs. 2 and 5) imply that rupture on the deeper, near vertical, western primary fault segment propagated towards the west and upwards onto a south-dipping plane without reaching the surface, with east plunging, oblique, left-lateral slip. (The NSL-RMT does not show plunging slip, perhaps because it use higher-frequency waves and close stations in a complex tectonic area, leading to poor resolution of shallower slip, and mainly showing horizontal slip of the earlier, deeper rupture.) The top of this shallow, south-dipping plane falls along the northwestern boundary of the main lobe of vertical subsidence and along a NE-SW trend of post-mainshock deformation identified in Sentinel-1 InSAR LOS displacement (*76*), as well as defining the southern boundary of a high density, NE-SW zone of mapped surface ruptures and fractures (*77*). This mainshock rupture evolution to the west likely caused large shallow slip, upwards rupture directivity and high shaking intensity, which could explain the large lobe of vertical subsidence and the after-slip identified in InSAR LOS displacement, as well as the abundant surface ruptures and fracturing along and to the north of this trend. Alternatively, the surface ruptures and fracturing may indicate shallow, a-seismic slip around the northern projection of the rupture plane. Thus mainshock rupture into the extensive, shallow, western damage zones may have produced greater shaking and potential damage than waves radiated from deeper slip on the two primary, en-echelon rupture surfaces.

Identification, study and understanding of earthquakes on relatively simple and isolated, but complete shear-crack systems such as Monte Cristo is important for identifying primary

causes of damaging earthquake shaking and mitigating earthquake hazard. Strong earthquakes around M 6-7 are much more frequent than major and great earthquakes and are thus more likely near and within urban areas, where they are recognized as a hazard on blind thrusts (*90, 91*). Strong earthquakes on large, possibly unidentified or hidden, shear-crack structures, with enhanced shaking and surface fracturing from extensive, associated damage zones, especially if shallow, may form a major part of the earthquake hazard in many areas.

High precision, absolute relocation of the 2020 Monte Cristo earthquake sequence clearly illustrates large earthquake rupture on a complete shear-crack system. This detailed seismicity, along with other geophysical and geological evidence, allows a comprehensive description of a complex rupture scenario for Monte Cristo within the framework of the shear-crack paradigm. These results emphasize the importance of using the complete shear-crack model to advance quantitative, monitoring and hazard seismology.

DATA AND RESOURCES

The supplementary material for this article includes: details on the NLL-SSST and NLL-SSST-coherence relocation procedures and FMAMP focal mechanisms, figures showing the velocity model used for location, epicentral maps for the USGS-NSL catalog and the different stages of NLL-SSST-coherence relocations of Monte Cristo seismicity, and foreshock and mainshock relocations, a 3D, fly-around animation of the NLL-SSST-coherence relocations of Monte Cristo seismicity, and an archive containing the NLL-SSST-coherence earthquake relocation catalog.

The USGS-NSL earthquake catalog and corresponding phase picks accessed from https://earthquake.usgs.gov (last accessed October 2020). The facilities of IRIS Data Services, and specifically the IRIS Data Management Center, were used for access to waveforms and related metadata used in this study. IRIS Data Services are funded through the Seismological Facilities for the Advancement of Geoscience and EarthScope (SAGE) Proposal of the National Science Foundation under Cooperative Agreement EAR-1261681. The U.S. Geological Survey and Nevada Bureau of Mines and Geology, Quaternary fault and fold database for the United States, is available at: https://www.usgs.gov/natural-hazards/earthquake-hazards/faults (last accessed October 2020).

All earthquake relocations were performed with NonLinLoc (*43, 92*) (http://www.alomax.net/nlloc, https://github.com/alomax/NonLinLoc). SeismicityViewer (http://www.alomax.net/software, last accessed October 2020) was used for 3D seismicity analysis and plotting, SeisGram2K (http://www.alomax.net/software, last accessed October 2020) was used for seismogram analysis and plotting, ObsPy (*93, 94*), (http://obspy.org, last accessed October 2020) for reading seismicity catalogs, EQcorrscan (*95*), (https://github.com/eqcorrscan/EQcorrscan, last accessed October 2020) for coherence calculations, and LibreOffice (https://www.libreoffice.org, last accessed October 2020) for word processing, spreadsheet calculations and charts.

REFERENCES

1.   T. Granier, Origin, damping, and pattern of development of faults in granite. *Tectonics*. **4**, 721–737 (1985).

2.   Y.-S. Kim, D. C. P. Peacock, D. J. Sanderson, Fault damage zones. *Journal of Structural Geology*. **26**, 503–517 (2004).

3.   T. M. Mitchell, D. R. Faulkner, The nature and origin of off-fault damage surrounding strike-slip fault zones with a wide range of displacements: A field study from the Atacama fault system, northern Chile. *Journal of Structural Geology*. **31**, 802–816 (2009).

4.   J.-H. Choi, P. Edwards, K. Ko, Y.-S. Kim, Definition and classification of fault damage zones: A review and a new methodological approach. *Earth-Science Reviews*. **152**, 70–87 (2016).

5.   C. Perrin, I. Manighetti, J.-P. Ampuero, F. Cappa, Y. Gaudemer, Location of largest earthquake slip and fast rupture controlled by along-strike change in fault structural maturity due to fault growth: EARTHQUAKE SLIP LINKED TO FAULT GROWTH. *J. Geophys. Res. Solid Earth*. **121**, 3666–3685 (2016).

6.   C. H. Scholz, *The Mechanics of Earthquakes and Faulting* (Cambridge University Press, Cambridge, ed. 3, 2019; https://www.cambridge.org/core/books/mechanics-of-earthquakes-and-faulting/ DEABA968016E051C9938E04B041945C2).

7.   H. Cloos, Experimente zur inneren Tektonik. *Centralblatt für Mineralogie*. **12**, 609–621 (1928).

8.   W. Riedel, Zur Mechanik geologischer Brucherscheinungen. *Centralblatt für Mineralogie*. **Abteilung B**, 354–368 (1929).

9.   W. F. Brace, E. G. Bombolakis, A note on brittle crack growth in compression. *Journal of Geophysical Research (1896-1977)*. **68**, 3709–3713 (1963).

10.   R. Madariaga, Dynamics of an expanding circular fault. *Bulletin of the Seismological Society of America*. **66**, 639–666 (1976).

11.   A. McGarr, D. D. Pollard, N. C. Gay, W. D. Ortlepp, in *Proceedings of Conference VIII: Analysis of Actual Fault Zones in Bedrock* (U. S. Geol. Survey, Menlo Park, 1979), *Open file Rep.*, pp. 101–120.

12.   P. Segall, D. D. Pollard, Nucleation and growth of strike slip faults in granite. *J. Geophys. Res.* **88**, 555 (1983).

13.   R. H. Sibson, Stopping of earthquake ruptures at dilational fault jogs. *Nature*. **316**, 248–251 (1985).

14.   F. M. Chester, J. M. Logan, Implications for mechanical properties of brittle faults from observations of the Punchbowl fault zone, California. *PAGEOPH*. **124**, 79–106 (1986).

15.   S. J. D. Cox, C. H. Scholz, On the formation and growth of faults: an experimental study. *Journal of Structural Geology*. **10**, 413–430 (1988).

16.   A. G. Sylvester, Strike-slip faults. *GSA Bulletin*. **100**, 1666–1703 (1988).

17.   J. Evans, Z. K. Shipton, Pachell, S. Lim, K. Robeson, in *In Proc. of the 3rd Confer. on Tecto. problems of the San Andreas system* (Stanford University, 2000).

18.   Y.-S. Kim, D. C. P. Peacock, D. J. Sanderson, Mesoscale strike-slip faults and damage zones at Marsalforn, Gozo Island, Malta. *Journal of Structural Geology*. **25**, 793–812 (2003).

19.   T. P. Dooley, G. Schreurs, Analogue modelling of intraplate strike-slip tectonics: A review and new experimental results. *Tectonophysics*. **574–575**, 1–71 (2012).

20.   Y. Klinger, K. Okubo, A. Vallage, J. Champenois, A. Delorme, E. Rougier, Z. Lei, E. E. Knight, A. Munjiza, C. Satriano, S. Baize, R. Langridge, H. S. Bhat, *Geophysical Research Letters*, in press, doi:10.1029/2018GL078842.

21. Y. Finzi, E. H. Hearn, Y. Ben-Zion, V. Lyakhovsky, Structural Properties and Deformation Patterns of Evolving Strike-slip Faults: Numerical Simulations Incorporating Damage Rheology. *Pure appl. geophys.* **166**, 1537–1573 (2009).

22. A. G. McGrath, I. Davison, Damage zone geometry around fault tips. *Journal of Structural Geology*. **17**, 1011–1024 (1995).

23. E. J. M. Willemse, D. D. Pollard, On the orientation and patterns of wing cracks and solution surfaces at the tips of a sliding flaw or fault. *J. Geophys. Res.* **103**, 2427–2438 (1998).

24. N. Christie-Blick, K. T. Biddle, in *Strike-Slip Deformation, Basin Formation, and Sedimentation*, K. T. Biddle, N. Christie-Blick, Eds. (SEPM Society for Sedimentary Geology, 1985; https://doi.org/10.2110/pec.85.37.0001), vol. 37, p. 0.

25. S. Das, C. Henry, Spatial relation between main earthquake slip and its aftershock distribution. *Reviews of Geophysics*. **41** (2003), doi:10.1029/2002RG000119.

26. C. Mendoza, S. H. Hartzell, Aftershock patterns and main shock faulting. *Bulletin of the Seismological Society of America*. **78**, 1438–1449 (1988).

27. N. Wetzler, T. Lay, E. E. Brodsky, H. Kanamori, Systematic deficiency of aftershocks in areas of high coseismic slip for large subduction zone earthquakes. *Science Advances*. **4**, eaao3225 (2018).

28. J. Woessner, D. Schorlemmer, S. Wiemer, P. M. Mai, Spatial correlation of aftershock locations and on-fault main shock properties. *Journal of Geophysical Research: Solid Earth*. **111** (2006), doi:10.1029/2005JB003961.

29. M. W. Stirling, S. G. Wesnousky, K. Shimazaki, Fault trace complexity, cumulative slip, and the shape of the magnitude-frequency distribution for strike-slip faults: a global survey. *Geophysical Journal International*. **124**, 833–868 (1996).

30. L. Chiaraluce, L. Valoroso, D. Piccinini, R. Di Stefano, P. De Gori, The anatomy of the 2009 L'Aquila normal fault system (central Italy) imaged by high resolution foreshock and aftershock locations. *J. Geophys. Res.* **116**, B12311 (2011).

31. E. Gràcia, I. Grevemeyer, R. Bartolomé, H. Perea, S. Martínez-Loriente, L. Gómez de la Peña, A. Villaseñor, Y. Klinger, C. Lo Iacono, S. Diez, A. Calahorrano, M. Camafort, S. Costa, E. d'Acremont, A. Rabaute, C. R. Ranero, Earthquake crisis unveils the growth of an incipient continental fault system. *Nature Communications*. **10**, 3482 (2019).

32. K. A. Kroll, E. S. Cochran, K. B. Richards‒Dinger, D. F. Sumy, Aftershocks of the 2010 Mw 7.2 El Mayor-Cucapah earthquake reveal complex faulting in the Yuha Desert, California. *Journal of Geophysical Research: Solid Earth*. **118**, 6146–6164 (2013).

33. P. Reasenberg, W. L. Ellsworth, Aftershocks of the Coyote Lake, California, earthquake of August 6, 1979: A detailed study. *J. Geophys. Res.* **87**, 10637–10655 (1982).

34. Z. E. Ross, E. S. Cochran, D. T. Trugman, J. D. Smith, 3D fault architecture controls the dynamism of earthquake swarms. *Science*. **368**, 1357–1361 (2020).

35. C. J. Ruhl, R. E. Abercrombie, K. D. Smith, I. Zaliapin, Complex spatiotemporal evolution of the 2008 Mw 4.9 Mogul earthquake swarm (Reno, Nevada): Interplay of fluid and faulting. *J. Geophys. Res. Solid Earth*. **121**, 8196–8216 (2016).

36. D. R. Shelly, W. L. Ellsworth, D. P. Hill, Fluid-faulting evolution in high definition: Connecting fault structure and frequency-magnitude variations during the 2014 Long Valley Caldera, California, earthquake swarm: Fluid-Faulting Evolution in Long Valley. *J. Geophys. Res. Solid Earth*. **121**, 1776–1795 (2016).

37. L. Valoroso, L. Chiaraluce, C. Collettini, Earthquakes and fault zone structure. *Geology*. **42**, 343–346 (2014).

38. F. Waldhauser, W. L. Ellsworth, *Journal of Geophysical Research: Solid Earth*, in press, doi:10.1029/2000JB000084.

39. S. G. Wesnousky, Active faulting in the Walker Lane. *Tectonics*. **24** (2005), doi:10.1029/2004TC001645.

40. K. DeLano, J. Lee, R. Roper, A. Calvert, Dextral, normal, and sinistral faulting across the eastern California shear zone–Mina deflection transition, California-Nevada, USA. *Geosphere*. **15**, 1206–1239 (2019).

41. G. A. Ichinose, J. G. Anderson, K. D. Smith, Y. Zeng, Source Parameters of Eastern California and Western Nevada Earthquakes from Regional Moment Tensor Inversion. *Bulletin of the Seismological Society of America*. **93**, 61–84 (2003).

42. A. Lomax, J. Virieux, P. Volant, C. Berge-Thierry, in *Advances in Seismic Event Location*, C. H. Thurber, N. Rabinowitz, Eds. (Springer Netherlands, Dordrecht, 2000; http://link.springer.com/10.1007/978-94-015-9536-0_5), vol. 18 of *Modern Approaches in Geophysics*, pp. 101–134.

43. A. Lomax, A. Michelini, A. Curtis, in *Encyclopedia of Complexity and Systems Science*, R. A. Meyers, Ed. (Springer New York, New York, NY, 2014; http://link.springer.com/10.1007/978-3-642-27737-5_150-2), pp. 1–33.

44. H. Benz, Building a National Seismic Monitoring Center: NEIC from 2000 to the Present. *Seismological Research Letters*. **88**, 265–269 (2017).

45. G. L. Pavlis, Appraising earthquake hypocenter location errors: A complete, practical approach for single-event locations. *Bulletin of the Seismological Society of America*. **76**, 1699–1717 (1986).

46. S. D. Billings, M. S. Sambridge, B. L. N. Kennett, Errors in hypocenter location: Picking, model, and magnitude dependence. *Bulletin of the Seismological Society of America*. **84**, 1978–1990 (1994).

47. J. Hardebeck, S. Husen, Earthquake location accuracy (2010), doi:10.5078/CORSSA-55815573.

48. J. S. Buehler, P. M. Shearer, Characterizing Earthquake Location Uncertainty in North America Using Source–Receiver Reciprocity and USArrayShort. *Bulletin of the Seismological Society of America*. **106**, 2395–2401 (2016).

49. V. Ryaboy, D. R. Baumgardt, P. Firbas, A. M. Dainty, Application of 3-D Crustal and Upper Mantle Velocity Model of North America for Location of Regional Seismic Events. *Pure appl. geophys.* **158**, 79–103 (2001).

50. M. Wagner, S. Husen, A. Lomax, E. Kissling, D. Giardini, High-precision earthquake locations in Switzerland using regional secondary arrivals in a 3-D velocity model. *Geophysical Journal International*. **193**, 1589–1607 (2013).

51. A. Darold, A. Holland, C. Chen, A. Youngblood, "Preliminary Analysis of Seismicity Near Eagleton 1-29, Carter County, July 2014" (Open-File Report OF2-2014, Oklahoma Geolical Survey, 2014), (available at http://ogs.ou.edu/docs/openfile/OF2-2014.pdf).

52. D. Latorre, F. Mirabella, L. Chiaraluce, F. Trippetta, A. Lomax, Assessment of earthquake locations in 3−D deterministic velocity models: A case study from the Altotiberina Near Fault Observatory (Italy). *J. Geophys. Res. Solid Earth*. **121**, 8113–8135 (2016).

53. I. Bondár, S. C. Myers, E. R. Engdahl, E. A. Bergman, Epicentre accuracy based on seismic network criteria. *Geophysical Journal International*. **156**, 483–496 (2004).

54. I. Bondar, K. McLaughlin, Seismic Location Bias and Uncertainty in the Presence of Correlated and Non-Gaussian Travel-Time Errors. *Bulletin of the Seismological Society of America*. **99**, 172–193 (2009).

55. S. C. Myers, Improving Sparse Network Seismic Location with Bayesian Kriging and Teleseismically Constrained Calibration Events. *Bulletin of the Seismological Society of America*. **90**, 199–211 (2000).

56. K. B. Richards-Dinger, P. M. Shearer, Earthquake locations in southern California obtained using source-specific station terms. *J. Geophys. Res.* **105**, 10939–10960 (2000).

57. A. Lomax, Location of the Focus and Tectonics of the Focal Region of the California Earthquake of 18 April 1906. *Bulletin of the Seismological Society of America*. **98**, 846–860 (2008).

58. A. Lomax, Absolute Location of 2019 Ridgecrest Seismicity Reveals a Shallow Mw 7.1 Hypocenter, Migrating and Pulsing Mw 7.1 Foreshocks, and Duplex Mw 6.4 Ruptures. *Bulletin of the Seismological Society of America*. **110**, 1845–1858 (2020).

59. T. Nicholson, D. Clarke, J. Townend, Regional earthquake location using empirical traveltimes in a region of strong lateral velocity heterogeneity. *Geophys J Int*. **175**, 560–570 (2008).

60. P. M. Shearer, Improving local earthquake locations using the L1 norm and waveform cross correlation: Application to the Whittier Narrows, California, aftershock sequence. *J. Geophys. Res.* **102**, 8269–8283 (1997).

61. J.-L. Got, J. Fréchet, F. W. Klein, Deep fault plane geometry inferred from multiplet relative relocation beneath the south flank of Kilauea. *J. Geophys. Res.* **99**, 15375 (1994).

62. P. Shearer, Southern California Hypocenter Relocation with Waveform Cross-Correlation, Part 2: Results Using Source-Specific Station Terms and Cluster Analysis. *Bulletin of the Seismological Society of America*. **95**, 904–915 (2005).

63. F. Waldhauser, A Double-Difference Earthquake Location Algorithm: Method and Application to the Northern Hayward Fault, California. *Bulletin of the Seismological Society of America*. **90**, 1353–1368 (2000).

64. G. Lin, P. M. Shearer, E. Hauksson, Applying a three-dimensional velocity model, waveform cross correlation, and cluster analysis to locate southern California seismicity from 1981 to 2005. *J. Geophys. Res.* **112**, B12309 (2007).

65. D. T. Trugman, P. M. Shearer, GrowClust: A Hierarchical Clustering Algorithm for Relative Earthquake Relocation, with Application to the Spanish Springs and Sheldon, Nevada, Earthquake Sequences. *Seismological Research Letters*. **88**, 379–391 (2017).

66. H. Zhou, Rapid three-dimensional hypocentral determination using a master station method. *J. Geophys. Res.* **99**, 15439 (1994).

67. Y. Font, H. Kao, S. Lallemand, C.-S. Liu, L.-Y. Chiao, Hypocentre determination offshore of eastern Taiwan using the Maximum Intersection method. *Geophysical Journal International*. **158**, 655–675 (2004).

68. A. Lomax, A Reanalysis of the Hypocentral Location and Related Observations for the Great 1906 California Earthquake. *Bulletin of the Seismological Society of America*. **95**, 861–877 (2005).

69. D. H. von Seggern, J. G. Anderson, I. M. Tibuleac, G. P. Biasi, Double-Difference Location and Ground-Truth Classification of the 2008 Mogul, Nevada, Very Shallow Earthquake Sequence. *Seismological Research Letters*. **86**, 146–157 (2015).

70. P. Podvin, I. Lecomte, Finite difference computation of traveltimes in very contrasted velocity models: a massively parallel approach and its associated tools. *Geophysical Journal International*. **105**, 271–284 (1991).

71. R. J. Geller, C. S. Mueller, Four similar earthquakes in central California. *Geophys. Res. Lett.* **7**, 821–824 (1980).

72. G. Poupinet, F. Glangeaud, P. Cote, in *ICASSP '82. IEEE International Conference on Acoustics, Speech, and Signal Processing* (Institute of Electrical and Electronics Engineers, Paris, France, 1982; http://ieeexplore.ieee.org/document/1171796/), vol. 7, pp. 1516–1519.

73. G. Poupinet, W. L. Ellsworth, J. Frechet, Monitoring velocity variations in the crust using earthquake doublets: An application to the Calaveras Fault, California. *J. Geophys. Res.* **89**, 5719–5731 (1984).

74. K. Rybicki, Analysis of aftershocks on the basis of dislocation theory. *Physics of the Earth and Planetary Interiors*. **7**, 409–422 (1973).

75. J. Liu, K. Sieh, E. Hauksson, A Structural Interpretation of the Aftershock "Cloud" of the 1992 Mw 7.3 Landers Earthquake, 12 (1992).

76. S. Valkaniotis, Interferograms for Monte Cristo EQ (2020), (available at https://doi.org/10.5281/zenodo.4273764).

77. A. J. Elliott, Dee, S., Koehler, R. D., Barnhart, W. D., Briggs, R., Collett, C., Dawson, T., DeLong, S., Gold, R. D., Haddon, E. K., Hartsorn, E., Hatem, A. E., Milliner, C., Pickering, A., Pierce, I., Seitz, G. G., Trexler, C., Wicks, C., Xu, X., & Zachariasen, J., Comparison of ground-based and space-based surface rupture mapping of the May 15, 2020 M6.5 Monte Cristo Range earthquake, Nevada. (2020), (available at https://www.scec.org/publication/10489).

78. C. Perrin, I. Manighetti, Y. Gaudemer, Off-fault tip splay networks: A genetic and generic property of faults indicative of their long-term propagation. *Comptes Rendus Geoscience*. **348**, 52–60 (2016).

79. D. A. Dodge, G. C. Beroza, W. L. Ellsworth, Detailed observations of California foreshock sequences: Implications for the earthquake initiation process. *J. Geophys. Res.* **101**, 22371–22392 (1996).

80. W. L. Ellsworth, F. Bulut, Nucleation of the 1999 Izmit earthquake by a triggered cascade of foreshocks. *Nature Geosci*. **11**, 531–535 (2018).

81. M. G. Stevens, "Candelaria Project Technical Report" (9814.00e, Silver Standard Resources, Pincock, Allen & Holt, Denver, Colorado, 2001), p. 62.

82. R. C. Speed, A. H. Cogbill, Candelaria and other left-oblique slip faults of the Candelaria region, Nevada. *GSA Bulletin*. **90**, 149–163 (1979).

83. J. W. Bell, C. Depolo, A. R. Ramelli, A. Sarna-Wojcicki, C. Meyer, Surface faulting and paleoseismic history of the 1932 Cedar Mountain earthquake area, west-central Nevada, and implications for modern tectonics of the Walker Lane. *Geological Society of America Bulletin*. **111**, 791–807 (1999).

84. S. G. Wesnousky, Seismological and structural evolution of strike-slip faults. *Nature*. **335**, 340–343 (1988).

85. R. Madariaga, High frequency radiation from dynamic earthquake fault models. *Annales de Geophysique*. **1**, 17–23 (1983).

86. M. Adda-Bedia, R. Madariaga, Seismic Radiation from a Kink on an Antiplane Fault. *Bulletin of the Seismological Society of America*. **98**, 2291–2302 (2008).

87. T. Uchide, H. Yao, P. M. Shearer, Spatio-temporal distribution of fault slip and high-frequency radiation of the 2010 El Mayor-Cucapah, Mexico earthquake. *Journal of Geophysical Research: Solid Earth*. **118**, 1546–1555 (2013).

88. T. Huang, H. Yao, Coseismic Radiation of the 2008 Mw 7.9 Wenchuan Earthquake and Its Relationship to Fault Complexities. *Pure Appl. Geophys*. **176**, 1207–1224 (2019).

89. Y.-S. Kim, D. J. Sanderson, in *Structural Geology: New Research*, S. J. Landowe, G. M. Hammler, Ed. (Nova Science, 2008), p. 19.

90. J. H. Shaw, J. Suppe, Earthquake hazards of active blind-thrust faults under the central Los Angeles basin, California. *Journal of Geophysical Research: Solid Earth*. **101**, 8623–8642 (1996).

91. E. H. Field, G. P. Biasi, P. Bird, T. E. Dawson, K. R. Felzer, D. D. Jackson, K. M. Johnson, T. H. Jordan, C. Madden, A. J. Michael, K. R. Milner, M. T. Page, T. Parsons, P. M. Powers, B. E. Shaw, W. R. Thatcher, R. J. Weldon II, Y. Zeng, "Uniform California earthquake rupture forecast, version 3 (UCERF3): the time-independent model," *Open-File Report* (USGS Numbered Series 2013–1165, U.S. Geological Survey, Reston, VA, 2013), p. 115.

92. A. Lomax, A. Zollo, P. Capuano, J. Virieux, Precise, absolute earthquake location under Somma-Vesuvius volcano using a new three-dimensional velocity model. *Geophysical Journal International*. **146**, 313–331 (2001).

93. M. Beyreuther, R. Barsch, L. Krischer, T. Megies, Y. Behr, J. Wassermann, ObsPy: A Python Toolbox for Seismology. *Seismological Research Letters*. **81**, 530–533 (2010).

94. L. Krischer, T. Megies, R. Barsch, M. Beyreuther, T. Lecocq, C. Caudron, J. Wassermann, ObsPy: a bridge for seismology into the scientific Python ecosystem. *Comput. Sci. Disc.* **8**, 014003 (2015).

95. C. J. Chamberlain, C. J. Hopp, C. M. Boese, E. Warren−Smith, D. Chambers, S. X. Chu, K. Michailos, J. Townend, EQcorrscan: Repeating and Near−Repeating Earthquake Detection and Analysis in Python. *Seismological Research Letters*. **89**, 173–181 (2018).